

Second-order correlated interference with multi-wavelength thermal-light beams

De-Sheng Wang(王德胜), Yi-Ning Zhao(赵一宁), Lingxin Kong(孔令鑫), Su-Heng Zhang(张素恒), Chong Wang(王翀), Cheng Ren(任承), Yuehua Su(苏跃华), and De-Zhong Cao(曹德忠)
Citation: Chin. Phys. B, 2026, 35 (**2**): 024201. DOI: 10.1088/1674-1056/ae1c31
http://cpb.iphy.ac.cn; http://iopscience.iop.org/cpb

What follows is a list of articles you may be interested in

Imaging a periodic moving/state-changed object with Hadamard-based computational ghost imaging

Hui Guo(郭辉), Le Wang(王乐), and Sheng-Mei Zhao(赵生妹)
Chin. Phys. B, 2022, 31 (**8**): 084201. DOI: 10.1088/1674-1056/ac6498

Nonclassicality of photon-modulated spin coherent states in the Holstein—Primakoff realization

Xiaoyan Zhang(张晓燕), Jisuo Wang(王继锁), Lei Wang(王磊),Xiangguo Meng(孟祥国), and Baolong Liang(梁宝龙)
Chin. Phys. B, 2022, 31 (**5**): 054205. DOI: 10.1088/1674-1056/ac40f5

Quantum statistical properties of photon-added spin coherent states

G Honarasa
Chin. Phys. B, 2017, 26 (**11**): 114202. DOI: 10.1088/1674-1056/26/11/114202

Lensless ghost imaging through the strongly scattering medium

Zhe Yang(杨哲), Lianjie Zhao(赵连洁), Xueliang Zhao(赵学亮), Wei Qin(秦伟), Junlin Li(李俊林)
Chin. Phys. B, 2016, 25 (**2**): 024202. DOI: 10.1088/1674-1056/25/2/024202

Phase modulation pseudocolor encoding ghost imaging

Duan De-Yang (段德洋), Zhang Lu (张路), Du Shao-Jiang (杜少将), Xia Yun-Jie (夏云杰)
Chin. Phys. B, 2015, 24 (**2**): 024202. DOI: 10.1088/1674-1056/24/2/024202

Second-order correlated interference with multi-wavelength thermal-light beams

De-Sheng Wang(王德胜)[1], Yi-Ning Zhao(赵一宁)[1], Lingxin Kong(孔令鑫)[1], Su-Heng Zhang(张素恒)[2], Chong Wang(王翀)[1], Cheng Ren(任承)[1], Yuehua Su(苏跃华)[1], and De-Zhong Cao(曹德忠)[1,†]

[1] *Department of Physics, Yantai University, Yantai* 264005, *China*
[2] *College of Physics Science & Technology, Hebei University, Baoding* 071002, *China*

(Received 17 September 2025; revised manuscript received 4 November 2025; accepted manuscript online 6 November 2025)

A method for correlating thermal light over a wide spectral range is proposed. A multi-wavelength pseudothermal source, prepared by projecting laser beams of multiple wavelengths (650 nm, 635 nm, 532 nm, and 473 nm) onto a moving thin ground glass plate, is employed in a double-slit interference experiment. The ground glass plate induces random phase differences between light beams of different wavelengths passing through it. This initial random phase difference significantly influences the high-order intensity correlation functions of multi-wavelength thermal beams. Experimentally, second-order correlated interference patterns, including subwavelength interference, of pseudothermal beams with different wavelengths are observed in the intensity correlation measurements. This method facilitates applications of correlated thermal photons in quantum information processing and quantum imaging.

Keywords: correlated interference, multi-wavelength thermal light, second-order correlation function

PACS: 42.25.Hz, 42.50.St

DOI: 10.1088/1674-1056/ae1c31 **CSTR:** 32038.14.CPB.ae1c31

1. Introduction

Correlating photons is a crucial quantum technology for quantum computing, quantum communication and quantum imaging.[1–3] The nonlinear crystals of spontaneous parametric down-conversion (SPDC) are widely used sources for generating correlated photons,[4] which can form entangled photon pairs in polarization, time, or energy.[3,5] These entangled photons are essential for foundational investigations of the violation of Bell inequalities, which distinguish quantum correlations from local hidden-variable theories.[6–8] In quantum communication, entangled photons enable secure protocols such as quantum key distribution, where eavesdropping attempts disrupt entanglement and reveal intrusion.[9] Using shared entanglement of photon pairs and classical communication, quantum teleportation transfers an unknown quantum state between distant locations without physical transmission.[10] Additionally, entangled photons enhance imaging resolution beyond classical limits, as demonstrated in quantum lithography and entanglement-based microscopy.[11,12]

To overcome the extreme weakness of entangled two-photon pairs, bright entangled multi-photon sources have drawn much attention. Multi-photon bundle emission has been investigated with parity-symmetry protection,[13] by a Josephson photonic device,[14] via atomic coherence,[15] in a quantum Rabi model,[16] and in multi-photon Jaynes–Cummings models.[17,18] Dynamical emission of multi-photon bundles can be realized in a circuit quantum electrodynamical system.[19] The NOON states of multi-photon entanglement, as another type of bright source, can be directly generated with structured crystals and shaped pump beams.[20] The multi-photon NOON states can also be generated in a composite system of two Kerr-nonlinear resonators and a four-level qudit,[21] and by coherently modulated independent single-photon sources.[22] Bright entangled multi-photon sources can greatly improve quantum metrology[23] and multiphoton quantum sensing.[24] These sources also have a powerful ability to enhance multiple-phase estimation,[25] especially for reconfigurable phase contrast microscopy[26] and reducing the uncertainty product of coherent light.[27] As a result, quantum superresolution imaging[28,29] and quantum microscopy[30] have been developed by exploiting multiphoton entanglement.

Unlike entangled photons, thermal light photons exhibit classical correlations but can still produce striking quantum-like effects through higher-order intensity correlation measurements.[31–33] Specifically, ghost imaging reconstructs an object's image by correlating photons from two beams, one interacting with the target and the other serving as a reference, even though neither beam alone carries the target's spatial information. This effect, initially demonstrated with entangled photons,[34] was later replicated using thermal light, highlighting the role of intensity fluctuations in correlation-based imaging.[31,32] Similarly, ghost in-

†Corresponding author. E-mail: dzcao@ytu.edu.cn

© 2026 Chinese Physical Society and IOP Publishing Ltd. All rights, including for text and data mining, AI training, and similar technologies, are reserved.

terference leverages higher-order correlations to reproduce interference patterns, even though the interfering beams do not possess first-order coherence.[35] These phenomena highlight how classical correlations can mimic certain quantum effects.[36] In two-photon subwavelength interference,[37–40] the superresolved fringes demonstrate the potential of thermal or chaotic light for quantum lithography and breaking the diffraction limit. Higher-order correlations with thermal light can comprehensively simulate behaviors originally associated with EPR correlations.[41]

Recently, photon correlations of two-color light,[42–44] uncorrelated sources,[45–47] and dissimilar sources[48–51] have been widely explored. Techniques and systems including nondegenerate SPDC, cavity-enhanced SPDC, time-resolved photon counting detection, optomechanical dark-mode excitation, superluminescent diodes, Hong–Ou–Mandel (HOM) interferometers, and Mach–Zehnder interferometers have been involved. These investigations have greatly extended the practical applications of photon correlations in quantum and classical systems. However, it remains challenging to correlate thermal light photons of different wavelengths over a wide spectral range.

In this paper, we propose a method to correlate pseudothermal beams of arbitrary two wavelengths using only a moving plate of ground glass in a double-slit interference experiment. With the proposed method, correlated interference patterns between a thermal light beam of wavelength 650 nm and beams of wavelengths 635 nm, 532 nm, and 473 nm are observed by measuring their intensity correlation functions. In addition, subwavelength interference fringes at different wavelengths are obtained by setting different propagation distances. In the theoretical analysis, the ground glass plate induces a random phase difference between two beams of different wavelengths. This random phase difference governs the second-order correlation functions of multi-wavelength thermal light. Therefore, this method enables correlation of thermal photons over a wide spectral range.

Compared with previous studies, this work has significant advantages. First, we use a thin ground glass plate to correlate thermal light of different wavelengths. This method is free from techniques such as active feed-forward synchronization[43] and time-correlated single photon counting.[42–49] Second, owing to the simple setup, the correlation is highly effective between pseudothermal light of different wavelengths. The efficiency is higher than that of feeble biphotons from spontaneous parametric down-conversion,[42] quantum dots,[48,49] and atomic quantum nodes.[51] Third, the wavelength range of correlation is quite wide. Our work demonstrates that pseudothermal light with wavelengths ranging from 473 nm to 650 nm can be correlated with each other, far exceeding the schemes mentioned above.

2. Experimental results of correlated interference

Generally, thermal light sources, such as flames and the sun, emit light beams of various wavelengths. These beams of different wavelengths from a thermal source are independent of each other. Our method for generating correlated pseudothermal beams of different wavelengths is shown in the experimental setup depicted in Fig. 1. A polarized beam splitter (PBS1) is used to combine the input laser beams of two wavelengths. In one arm of PBS1, a fixed laser diode (LD) emits a laser beam of wavelength 650 nm. In the other arm, three LDs with wavelengths 635 nm, 532 nm, and 473 nm are prepared, and one of them is selected for each experiment. Both laser beams pass through a double-slit (DS) and a lens (L), and then arrive at PBS1. Two polarizers (P) are used to adjust the intensities of the two input laser beams. A thin plate of ground glass (GG), with only one side roughened by fine sandpaper, serves as a random-phase modulator. GG converts the two laser beams of different wavelengths into dynamic and correlated multi-wavelength laser speckles, which imitate the spatiotemporal behaviors of multi-wavelength thermal light. The outgoing polarized pseudothermal patterns are separated by another PBS2 and detected by two charge-coupled devices (CCD: Mintron MTV-1881EX). CCD1 and CCD2 register the instantaneous intensity distributions of pseudothermal light at wavelength 650 nm and at the other wavelengths (635 nm, 532 nm, 473 nm), respectively. Correlation measurements (CM) are performed between the two pseudothermal intensities to observe correlated interference fringes.

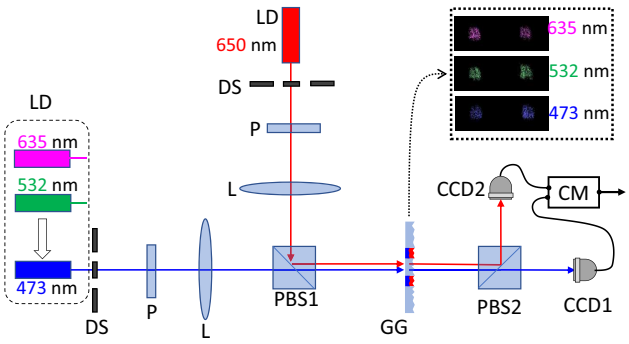


Fig. 1. Diagram of the experimental setup. A pseudothermal beam of wavelength 650 nm is correlated with beams of wavelengths 635 nm, 532 nm, and 473 nm. LD: laser diode; DS: double slit; P: polarizer; L: lens; PBS: polarized beam splitter; GG: ground glass; CCD: charge-coupled device; CM: correlation measurement.

The thin GG plate is mounted on a movable stage, which is driven by a stepper motor. To precisely control the phase modulation of GG, the frosted surface of GG is adjusted to face the detectors. Two double-slits, with a slit width of 60 μm, a spacing of 180 μm, and a height of 60 μm, are employed in the experiment. The two DS are imaged by the two lenses onto the frosted surface of GG. We note that the focal lengths of the lenses are 150.3 mm, 149.9 mm, 149.1 mm,

and 148.0 mm for wavelengths of 650 nm, 635 nm, 532 nm, and 473 nm, respectively. The optical paths in the two arms of PBS1 are carefully adjusted to ensure that the sizes of the two images of the DS are exactly the same. The microscopic images of the double slits at different wavelengths are shown in the inset of Fig. 1.

The experimental results of correlated fringes obtained from intensity correlation measurements of pseudothermal light beams at different wavelengths are shown in Fig. 2. The GG plate moves at a steady speed, ensuring that each of the two CCDs records 30 independent patterns per second. The distances from GG to the two CCDs are both set to $z = z' = 240$ mm.

Figure 2(a) shows the results for beam wavelengths of 650 nm and 635 nm with 20000 samples. In Fig. 2(a), the magenta circles and red squares represent the experimental data of the normalized second-order intensity correlation functions $g^{(2)}_{650,635}(0,x)$ and $g^{(2)}_{650,635}(x,0)$, respectively. Their maxima are 1.80 and 1.81, indicating that the corresponding fringe visibility values are $V = 0.281$ and 0.286. The magenta and red solid lines are the theoretical curves. In addition, the insets show the two-dimensional patterns. It can be seen that the two fringe spacings are nearly the same, $\Delta x_{650} = 0.640$ mm and $\Delta x_{635} = 0.630$ mm, since the two wavelengths are close.

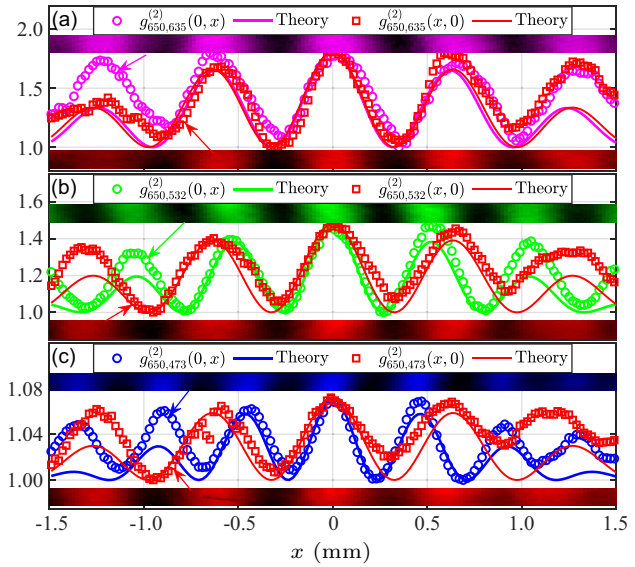


Fig. 2. Experimental results of the normalized intensity correlation functions for wavelength pairs 650–635 nm in (a), 650–532 nm in (b), and 650–473 nm in panel (c), respectively. The subimages show the two-dimensional distributions. The circles and squares represent the experimental results, and the solid lines denote the theoretical results.

Similarly, Fig. 2(b) shows the results for beam wavelengths 650 nm and 532 nm with 20000 samples. The green circles and red squares represent the experimental results of the one-dimensional normalized second-order correlation functions $g^{(2)}_{650,532}(0,x)$ and $g^{(2)}_{650,532}(x,0)$, respectively. Their maxima are 1.47 and 1.48, indicating fringe visibility values of $V = 0.190$ and 0.191. The two fringe spacings are different, $\Delta x_{650} = 0.645$ mm and $\Delta x_{532} = 0.525$ mm, since the wavelength difference becomes larger. The green and red solid lines are the corresponding theoretical curves.

Figure 2(c) presents the results for beam wavelengths 650 nm and 473 nm with 20000 samples. The blue circles and red squares represent the experimental results of the one-dimensional normalized second-order correlation functions $g^{(2)}_{650,473}(0,x)$ and $g^{(2)}_{650,473}(x,0)$, respectively. Their maxima are 1.071 and 1.072, and the corresponding fringe visibility values are $V = 0.0339$ and 0.0344. The two fringe spacings are different, $\Delta x_{650} = 0.630$ mm and $\Delta x_{473} = 0.443$ mm, since the wavelength difference is the largest. The blue and red solid lines are the corresponding theoretical curves.

The extremely low fringe visibility obtained from $g^{(2)}_{650,473}$ indicates stringent experimental conditions for second-order correlated interference with multi-wavelength thermal light. Indeed, the ground glass is one-sided frosted. After passing through the GG plate, the beam of wavelength λ undergoes a phase change $\phi(\lambda) = 2\pi\frac{n(\lambda)-1}{\lambda}\delta_0$, where n is the refractive index at wavelength λ, and δ_0 is the random depth of the glass divots.

3. Theory and subwavelength interference

To ensure stable intensity correlation between light beams of wavelengths λ and λ', the two phase changes should satisfy $\phi(\lambda) - \phi(\lambda') < 2\pi$ and $\phi(\lambda) + \phi(\lambda') \geq 2\pi$. In experiment, therefore, the average depth $\overline{\delta_0}$ of the glass divots should satisfy the condition

$$\frac{1}{\frac{n-1}{\lambda} + \frac{n'-1}{\lambda'}} < \overline{\delta_0} < \frac{1}{\left|\frac{n-1}{\lambda} - \frac{n'-1}{\lambda'}\right|}, \tag{1}$$

where n' is the refractive index of the glass for light of wavelength λ'. The condition in Eq. (1) limits the range of phase difference for a successful experiment; it is also the reason for the one-sided frosted GG mentioned above.

For complete incoherence of thermal light, the amplitudes and random phases of the thermal fields are regarded as stochastic variables, which follow the Rayleigh distribution and a uniform distribution, respectively. Without loss of generality, the total phase change is assumed to satisfy $\phi(\lambda) + \phi(\lambda') = 2m\pi$ for steady second-order interference fringes, where m is a positive integer. For mathematical simplicity, the double slit is considered as the sum of two single delta functions $D(x_0) = \delta(x_0 - d/2) + \delta(x_0 + d/2)$, where d is the slit spacing. Under these assumptions, the normalized second-order correlation function between thermal light beams of wavelengths λ and λ' is obtained as

$$g^{(2)}_{\lambda,\lambda'}(x,x') = \frac{3}{2} + \frac{\mathrm{sinc}(\Delta\varphi)}{2}\cos\left(\frac{2\pi\,\mathrm{d}x}{\lambda z} - \frac{2\pi\,\mathrm{d}x'}{\lambda' z'} + \Delta\varphi\right), \tag{2}$$

where z (z') is the propagation distance of light with wavelength λ (λ'), the sinc function is defined as $\mathrm{sinc}(\Delta\varphi) = \sin(\Delta\varphi)/\Delta\varphi$, and the phase difference is

$$\Delta\varphi = m\pi\frac{\frac{\lambda'}{\lambda}-\frac{n'-1}{n-1}}{\frac{\lambda'}{\lambda}+\frac{n'-1}{n-1}} = m\pi\frac{R_\lambda - R_n}{R_\lambda + R_n}, \tag{3}$$

where the wavelength ratio is $R_\lambda = \frac{\lambda'}{\lambda}$, and the refractive index ratio is $R_n = \frac{n'-1}{n-1}$. The fringe visibility of the normalized second-order correlation function is

$$V = \frac{1}{3}\left|\mathrm{sinc}(\Delta\varphi)\right|. \tag{4}$$

It is clear that as the wavelength difference $|\lambda - \lambda'|$ increases, the phase difference $\Delta\varphi$ also increases, whereas the fringe visibility V decreases.

The fringe spacings of the normalized correlated interference patterns in Fig. 2 are determined by the propagation distances and the corresponding wavelengths. This behavior is consistent with the theoretical prediction in Eq. (2). As the wavelength difference $|\lambda - \lambda'|$ increases, the phase difference $\Delta\varphi$ becomes larger, and the visibility V decreases. This conclusion is also demonstrated in Figs. 2 and 3.

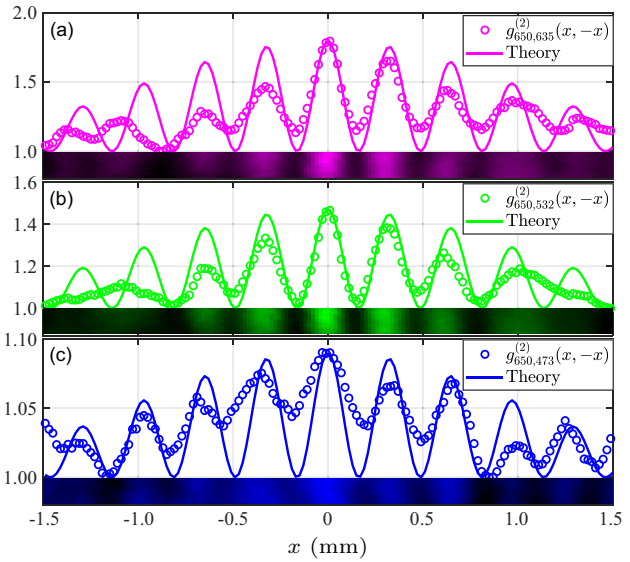


Fig. 3. Experimental results of the subwavelength interference fringes. (a) $g^{(2)}_{650,635}(x,-x)$ with $z_{635} = 245$ mm. (b) $g^{(2)}_{650,532}(x,-x)$ with $z_{532} = 296$ mm. (c) $g^{(2)}_{650,473}(x,-x)$ with $z_{473} = 326$ mm. The propagation distance is $z_{650} = 240$ mm, and the inset subimages show the two-dimensional distributions.

From the normalized second-order correlation function in Eq. (2), it can be seen that subwavelength interference can be obtained under the condition $x' = -\frac{\lambda' z'}{\lambda z}x$ for correlation measurements. By setting the propagation distance $z' = \frac{\lambda}{\lambda'}z$, the normalized intensity correlation function becomes $g^{(2)}_{\lambda,\lambda'}(x,-x) = \frac{3}{2} + \frac{\mathrm{sinc}(\Delta\varphi)}{2}\cos\left(\frac{2\pi d}{\lambda z}2x + \Delta\varphi\right)$, which manifests superresolved fringes. According to the condition of propagation distance, the experimental results of the subwavelength interference are shown in Fig. 3, where the propagation distance $z_{650} = 240$ mm is set for the thermal light beam of wavelength 650 nm. Figure 3(a) presents the subwavelength interference fringes of $g^{(2)}_{650,635}(x,-x)$, where the propagation distance $z' = 245$ mm is set for the thermal light of wavelength 635 nm. The magenta circles and solid line are the experimental data and the theoretical curve, respectively. It can be seen that the fringe spacing has been reduced by half to $\Delta x = 0.324$ mm.

The experimental results of subwavelength interference fringes between the thermal light beams of wavelengths 650 nm and those of 532 nm and 473 nm are respectively exhibited in Figs. 3(b) and 3(c), by the green and blue circles. The propagation distances for thermal beams of wavelength 532 nm and 473 nm are set as $z' = 296$ mm and 326 mm, respectively. Both of the fringe spacings are $\Delta x = 0.320$ mm for the interference patterns in Figs. 3(b) and 3(c).

In Fig. 3, the two-dimensional distributions of the second-order subwavelength interference patterns are shown by the subimages under the curves. The visibility values are $V = 0.286$, 0.184, 0.035 for the correlated interference fringes in Figs. 3(a)–3(c), respectively. The fringe visibility values in the three cases are similar to those in Fig. 2. However, the subwavelength feature of the halved fringe spacing is demonstrated by comparing it with the results in Fig. 2.

In practice, the random depths of the divots distributed in the GG plate cause phase differences and extra scattered noise, both of which strongly affect the second-order interference fringes between thermal beams of two wavelengths. In the numerical simulation, H-K9L glass is considered. The phase noise level is set as $1/10$ of the phase change for all pseudothermal beams. Figure 4 shows the numerical maximum values of the second-order correlation function $g^{(2)}_{\max}$ versus the average divot depth $\overline{\delta_0}$. The inset shows the details of the simulation results for the average divot depth in the range $0 < \overline{\delta_0} < 8$ μm. These maxima are the averages of 50 simulations, each of which is calculated with 20000 simulated samples. The magenta solid line with circles, green dashed line with squares, and blue dotted line with diamonds are the simulated maxima of $g^{(2)}_{650,635}$, $g^{(2)}_{650,532}$, and $g^{(2)}_{650,473}$, respectively.

As the average depth of the glass divots δ_0 increases, the maximum values $g^{(2)}_{\max}$ first rapidly rise from 1 to their maximum values, and then gradually decrease back to 1. The full widths at half maxima (FWHM) for $g^{(2)}_{650,635}$, $g^{(2)}_{650,532}$, and $g^{(2)}_{650,473}$ in Fig. 4 are 22.64 μm, 2.53 μm, and 1.61 μm, respectively. As the wavelength difference ($|\lambda - \lambda'|$) increases, the FWHM decreases, and the value of $g^{(2)}_{\max}(\lambda,\lambda')$ also decreases. By connecting the experimental and simulation results, it can be concluded that the average divot depth is about $\overline{\delta_0} = 2.0$ μm in our experiment.

This dependence of the second-order correlation maximum on wavelength suggests a non-destructive testing method for characterizing the microstructure of scattering surfaces,

such as ground glass. By injecting two probing beams of different wavelengths (λ and λ'), the surface feature scale δ_0 can be obtained by measuring the second-order correlation maxima $g^{(2)}_{\max}(\lambda,\lambda')$. This technique is particularly valid when the characteristic scale of the surface roughness is comparable to the incident wavelength.

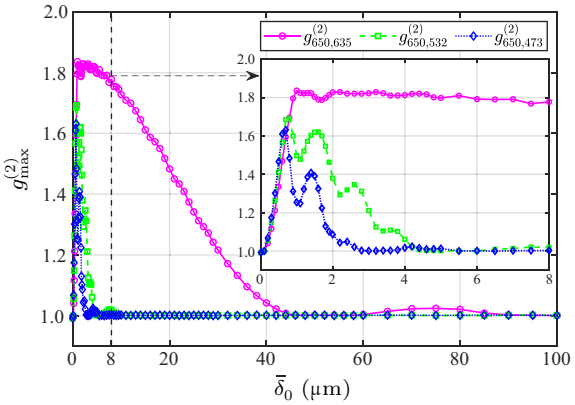


Fig. 4. Simulation results of the maxima of the normalized second-order correlation function $g^{(2)}_{\max}(\lambda,\lambda')$ versus the average divot depth δ_0. The magenta, green, and blue lines correspond to thermal light beams with $\lambda' = 635$ nm, 532 nm, and 473 nm, respectively, and $\lambda = 650$ nm. The inset plots the maxima in the range $0 < \bar{\delta}_0 < 8$.

4. Conclusion

In summary, the second-order correlated interference of wide-spectrum thermal beams has been investigated. Experimentally, multi-wavelength pseudothermal beams were generated by projecting laser beams of four wavelengths (650 nm, 635 nm, 532 nm, and 473 nm) onto a moving thin GG plate. The second-order correlated interference patterns between these multi-wavelength pseudothermal beams were characterized by measuring their intensity correlation functions. Subwavelength interference fringes were obtained by adjusting the propagation distances for the different wavelengths. The maxima of the normalized second-order correlation functions, fringe spacing, and fringe visibility depend on the wavelength differences and the phase differences induced by the GG. This method is effective for correlating thermal photons of various wavelengths. Although the proposed approach is limited by decreases in visibility, surface uniformity, and mechanical stability, it has potential applications in multi-wavelength ghost imaging, correlation-based spectroscopy, and broadband phase retrieval. Furthermore, it may expand the potential applications of thermal photons in quantum information processing and quantum imaging.

Appendix A: Probability theory of the random fields in double-slit interference

In our interference experiment with multi-wavelength thermal light beams, the local pieces of the ground glass are considered to be exactly embedded inside the double slits, as shown in Fig. A1. The random depths of the divots in the frosted surface of the ground glass plate play an important role in observing the correlated interference patterns in the experiment. Therefore, the divot depths in the slits can be regarded as stochastic variables.

For mathematical simplicity, we assume two stochastic variables r_{10} and r_{20} to describe the divot depths in the two slits when the ground glass plate moves, as shown in Fig. 1. Considering that the normal thickness of the glass is r_0, the optical paths of the light in the two slits are

$$\Delta_j = n r_{j0} + (r_0 - r_{j0}) = (n(\lambda) - 1) r_{j0} + r_0, \tag{A1}$$

where $j = 1,2$ refers to the respective slits, and n is the refractive index, which depends on the optical wavelength λ. The refractive index of 1 for the atmosphere has been assumed in Eq. (A1). The optical path difference of the two fields from the two slits is

$$\Delta_\lambda = \Delta_2 - \Delta_1 = (n(\lambda) - 1)(r_{20} - r_{10}) = (n(\lambda) - 1)\delta_0, \tag{A2}$$

where the subscript λ denotes the wavelength dependence of n. Since the divots r_{10} and r_{20} are completely random, their depth difference $\delta_0 = r_{20} - r_{10}$ is completely random as well.

The stable laser fields pass through the ground glass and then the two slits, and finally arrive at the screen after a distance z. At the point P on the screen, the two fields from the two slits are

$$E_j = A_j \, \mathrm{e}^{-\mathrm{i}\left(\omega t - \frac{2\pi r_j}{\lambda} - \frac{2\pi \Delta_j}{\lambda}\right)}, \tag{A3}$$

where $j = 1,2$, and r_1 and r_2 are the distances from the point P to the two slits, respectively. The summed field at the point P is $E = E_1 + E_2$, and the optical intensity is obtained as

$$I = |E|^2 = A_1^2 + A_2^2 + 2A_1A_2 \cos\left(2\pi \frac{\Delta_r + \Delta_\lambda}{\lambda}\right), \tag{A4}$$

where $\Delta_r = r_2 - r_1$. It can be seen that the intensity distribution depends strongly on the initial random phase $\frac{2\pi\Delta_\lambda}{\lambda} = \frac{2\pi}{\lambda}(n-1)\delta_0$.

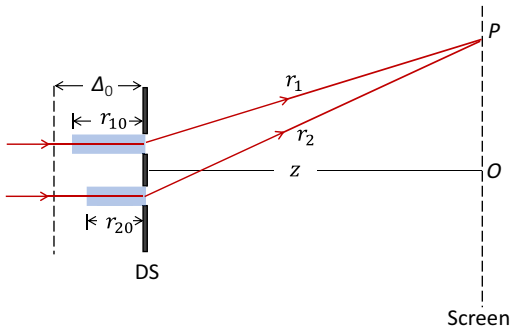


Fig. A1. Random phase distribution in a double-slit interference.

It is assumed that the amplitude A follows a Rayleigh distribution

$$P_A = \frac{A}{\sigma^2} \, \mathrm{e}^{-\frac{A^2}{2\sigma^2}}, \tag{A5}$$

where $A \geq 0$, and σ is the distribution parameter. The even-order and odd-order moments of the amplitude are

$$\begin{aligned}\left\langle A^{2m}\right\rangle &= m!\,2^m\sigma^{2m},\\ \left\langle A^{2m+1}\right\rangle &= (2m+1)!!\sqrt{\frac{\pi}{2}}\sigma^{2m+1},\end{aligned} \tag{A6}$$

where the factorials are $m! = 1\times 2\times 3\times\cdots\times m$ and $(2m+1)!! = 1\times 3\times 5\times\cdots\times(2m+1)$.

The path difference δ_0 is assumed to follow a uniform distribution such that

$$P_{\delta_0} = \frac{1}{2\pi}\mathrm{rect}\left(\frac{\delta_0-\pi}{2\pi}\right), \tag{A7}$$

where $\delta_0 \in [0, 2\pi]$, and $\mathrm{rect}(x) = \begin{cases}1, & |x|\leq 1/2\\ 0, & |x|>1/2\end{cases}$. The averages of the cosine function powers are

$$\left\langle\cos^{2m}\delta_0\right\rangle = 2^{-2m}C_{2m}^m,\ \left\langle\cos^{2m+1}\delta_0\right\rangle = 0. \tag{A8}$$

Appendix B: Intensity correlation function

According to Eqs. (A4), (A6), and (A8), the averaged intensity distribution is obtained as

$$\langle I\rangle = \left\langle A_1^2\right\rangle + \left\langle A_2^2\right\rangle = 4\sigma^2. \tag{B1}$$

The interference fringes do not appear on the detection plane, reflecting incoherent illumination.

Consider two different laser beams with wavelengths λ_1 and λ_2. The optical intensities for the two stochastic fields are

$$I_1 = A_1^2 + A_2^2 + 2A_1A_2\cos\left(2\pi\frac{\Delta_r+\Delta_{\lambda_1}}{\lambda_1}\right), \tag{B2}$$

$$I_2 = A_1'^2 + A_2'^2 + 2A_1'A_2'\cos\left(2\pi\frac{\Delta_r'+\Delta_{\lambda_2}}{\lambda_2}\right), \tag{B3}$$

where the optical path differences are approximately

$$\begin{aligned}&\Delta_r \approx \frac{\mathrm{d}x_1}{z_1},\quad \Delta_r' \approx \frac{\mathrm{d}x_2}{z_2},\\ &\Delta_{\lambda_1} = (n_{\lambda_1}-1)\delta_0,\quad \Delta_{\lambda_2} = (n_{\lambda_2}-1)\delta_0.\end{aligned} \tag{B4}$$

The average of the intensity correlation is

$$\begin{aligned}\langle I_1(x_1)I_2(x_2)\rangle =\ & \left\langle A_1^2A_1'^2 + A_1^2A_2'^2 + A_2^2A_1'^2 + A_2^2A_2'^2\right\rangle\\ &+4\left\langle A_1A_2A_1'A_2'\right\rangle\\ &\times\left\langle\cos 2\pi\left(\frac{\mathrm{d}x_1}{\lambda_1 z_1}+\delta_0\frac{n_{\lambda_1}-1}{\lambda_1}\right)\right.\\ &\left.\times\cos 2\pi\left(\frac{\mathrm{d}x_2}{\lambda_2 z_2}+\delta_0\frac{n_{\lambda_2}-1}{\lambda_2}\right)\right\rangle.\end{aligned} \tag{B5}$$

By assuming $A_1 = \beta A_1'$ and $A_2 = A_2'$, the moments of the amplitudes are

$$\left\langle A_1^2A_1'^2\right\rangle = \left\langle A_2^2A_2'^2\right\rangle = \beta^2\,8\sigma^4, \tag{B6}$$

$$\left\langle A_1^2A_2'^2\right\rangle = \left\langle A_2^2A_1'^2\right\rangle = \beta^2\,4\sigma^4, \tag{B7}$$

$$\left\langle A_1A_2A_1'A_2'\right\rangle = \beta^2\,4\sigma^4. \tag{B8}$$

The cosine-product term in Eq. (B5) can be rewritten as

$$\begin{aligned}&\left\langle\cos 2\pi\left(\frac{\mathrm{d}x_1}{\lambda_1 z_1}+\delta_0\frac{n_{\lambda_1}-1}{\lambda_1}\right)\cos 2\pi\left(\frac{\mathrm{d}x_2}{\lambda_2 z_2}+\delta_0\frac{n_{\lambda_2}-1}{\lambda_2}\right)\right\rangle\\ &= \frac{1}{2}\left\langle\cos 2\pi\left(\frac{\mathrm{d}x_1}{\lambda_1 z_1}+\frac{\mathrm{d}x_2}{\lambda_2 z_2}+\frac{n_{\lambda_1}-1}{\lambda_1}\delta_0+\frac{n_{\lambda_2}-1}{\lambda_2}\delta_0\right)\right\rangle\\ &\quad+\frac{1}{2}\left\langle\cos 2\pi\left(\frac{\mathrm{d}x_1}{\lambda_1 z_1}-\frac{\mathrm{d}x_2}{\lambda_2 z_2}+\frac{n_{\lambda_1}-1}{\lambda_1}\delta_0-\frac{n_{\lambda_2}-1}{\lambda_2}\delta_0\right)\right\rangle.\end{aligned} \tag{B9}$$

In Eq. (B9), the phase of the first cosine term fluctuates much faster than that of the second cosine term. We thus impose the condition

$$2\pi\delta_0\left(\frac{n_{\lambda_1}-1}{\lambda_1}+\frac{n_{\lambda_2}-1}{\lambda_2}\right) = 2m\pi, \tag{B10}$$

where m is an integer. Under this condition, the average of the first cosine term in Eq. (B9) vanishes, while the average of the second cosine term becomes

$$\begin{aligned}&\left\langle\cos\left[2\pi\left(\frac{\mathrm{d}x_1}{\lambda_1 z_1}-\frac{\mathrm{d}x_2}{\lambda_2 z_2}+\frac{n_{\lambda_1}-1}{\lambda_1}\delta_0-\frac{n_{\lambda_2}-1}{\lambda_2}\delta_0\right)\right]\right\rangle\\ &= \mathrm{sinc}(\Delta\varphi)\cos\left[2\pi d\left(\frac{x_1}{\lambda_1 z_1}-\frac{x_2}{\lambda_2 z_2}\right)+\Delta\varphi\right],\end{aligned} \tag{B11}$$

where

$$\Delta\varphi = k\pi\frac{\frac{n_{\lambda_1}-1}{\lambda_1}-\frac{n_{\lambda_2}-1}{\lambda_2}}{\frac{n_{\lambda_1}-1}{\lambda_1}+\frac{n_{\lambda_2}-1}{\lambda_2}} = k\pi\frac{R_\lambda-R_n}{R_\lambda+R_n}, \tag{B12}$$

$$R_\lambda = \frac{\lambda_2}{\lambda_1},\quad R_n = \frac{n_{\lambda_2}-1}{n_{\lambda_1}-1}. \tag{B13}$$

The nonzero average in Eq. (B11) represents the nonlocal interference fringes. Consequently, the intensity correlation function between the beams of different wavelengths is

$$\begin{aligned}\langle I_1(x_1)I_2(x_2)\rangle =\ & 24\beta^2\sigma^4 + 8\beta^2\sigma^4\mathrm{sinc}(\Delta\varphi)\\ &\times\cos\left(\frac{2\pi\,\mathrm{d}x_1}{\lambda_1 z_1}-\frac{2\pi\,\mathrm{d}x_2}{\lambda_2 z_2}+\Delta\varphi\right).\end{aligned} \tag{B14}$$

The normalized second-order correlation function is

$$\begin{aligned}g^{(2)}(x_1,x_2) &= \frac{\langle I_1(x_1)I_2(x_2)\rangle}{\langle I_1(x_1)\rangle\langle I_2(x_2)\rangle}\\ &= \frac{3}{2}+\frac{1}{2}\mathrm{sinc}(\Delta\varphi)\cos\left(\frac{2\pi\,\mathrm{d}x_1}{\lambda_1 z_1}-\frac{2\pi\,\mathrm{d}x_2}{\lambda_2 z_2}+\Delta\varphi\right).\end{aligned} \tag{B15}$$

Hence, the fringe visibility is

$$V = \frac{|\mathrm{sinc}(\Delta\varphi)|}{3}, \tag{B16}$$

since the maximum and minimum of the normalized second-order correlation function are $g^{(2)}_{\max} = \frac{3}{2}+\frac{1}{2}|\mathrm{sinc}(\Delta\varphi)|$ and $g^{(2)}_{\min} = \frac{3}{2}-\frac{1}{2}|\mathrm{sinc}(\Delta\varphi)|$, respectively.

Appendix C: The independent first-order and second-order correlation

The independent first-order correlation functions, i.e., the averaged intensity distributions, are shown in Fig. C1. The circles in Figs. C1(a)–C1(d) represent the experimental results of the averaged pseudothermal light intensity distributions for wavelengths 650 nm, 635 nm, 532 nm, and 473 nm, respectively.

The fluctuations of these averaged intensity distributions are all very small, and no interference fringes are observed. The corresponding fringe visibility values are 0.0149, 0.02494, 0.0251, and 0.0300, all of which are smaller than those in Figs. 2 and 3. These results indicate that the first-order coherence is very weak under the experimental conditions.

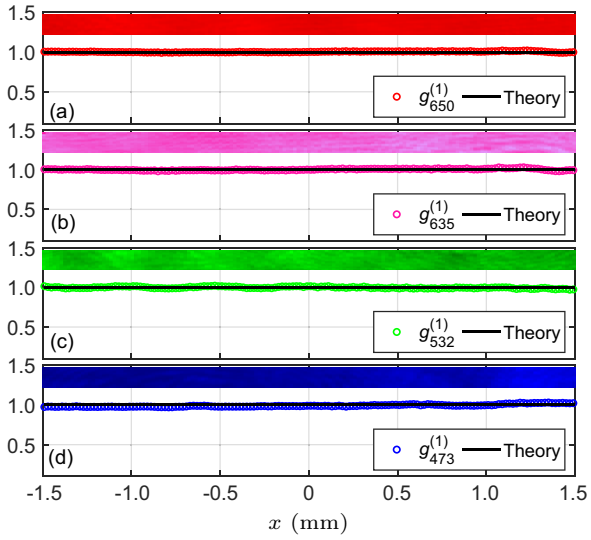


Fig. C1. The first-order correlation functions of pseudotherma light of wavelength (a) 650 nm, (b) 635 nm, (c) 532 nm, and (d) 473 nm.

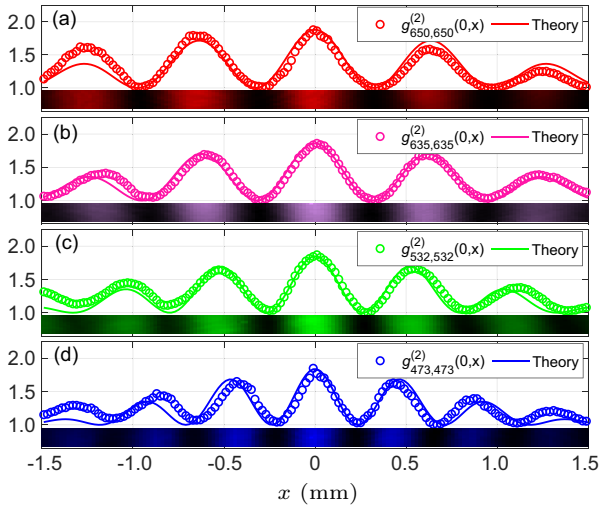


Fig. C2. The second-order correlation functions of pseudothermal light of wavelengths (a) 650 nm, (b) 635 nm, (c) 532 nm, and (d) 473 nm.

The second-order correlation functions of the pseudothermal light beams of the same wavelengths are shown in Fig. C2. The experimental results for wavelengths 650 nm, 635 nm, 532 nm, and 473 nm are represented by the circles in Figs. C2(a)–C2(d), with fringe maxima of 1.88, 1.86, 1.87, and 1.85, respectively.

These correlation maxima are all greater than 1 and close to 2. By comparing the first-order and second-order correlation functions, it is evident that the pseudothermal light in the experiment exhibits very low first-order coherence but strong second-order correlation.

Appendix D: Notes on numerical simulations

The ground glass (H-K9L) plate used in the experiment is also considered in the numerical simulations. The refractive index is modeled using the Cauchy dispersion equation

$$n=\sqrt{A_0+A_1\lambda^2+A_2\lambda^{-2}+A_3\lambda^{-4}+A_4\lambda^{-6}+A_5\lambda^{-8}},$$

where the constants are $A_0=2.2719694$, $A_1=-9.9172187\times10^{-3}$, $A_2=1.0369753\times10^{-2}$, $A_3=3.1190380\times10^{-4}$, $A_4=-2.6458215\times10^{-5}$, and $A_5=1.6479085\times10^{-6}$.

Acknowledgments

This work was supported by the National Natural Science Foundation of China (Grant Nos. 62105278 and 11674273) and the Natural Science Foundation of Shandong Province (Grant No. ZR2023MA015).

References

[1] Nielsen M A and Chuang I L 2010 *Quantum Computation and Quantum Information* (Cambridge: Cambridge University Press)
[2] Bennett C H and Brassard G 2014 *Theor. Comput. Sci.* **560** 7
[3] Zhang Z, You C, Magaña-Loaiza O S, Fickler R, León-Montiel R de J, Torres J P, Humble T S, Liu S, Xia Y and Zhuang Q 2024 *Adv. Opt. Photonics* **16** 60
[4] Kwiat P G, Mattle K, Weinfurter H, Zeilinger A, Sergienko A V and Shih Y 1995 *Phys. Rev. Lett.* **75** 4337
[5] Guo Y X, Xu X X, Chen Z P, Zhou Y G, Liu B, He H X, Li Y Y and Xie J N 2024 *Chin. Phys. Lett.* **41** 014201
[6] Aspect A, Dalibard J and Roger G 1982 *Phys. Rev. Lett.* **49** 1804
[7] Ou Z Y and Mandel L 1988 *Phys. Rev. Lett.* **61** 50
[8] Shih Y H and Alley C O 1988 *Phys. Rev. Lett.* **61** 2921
[9] Ekert A K 1991 *Phys. Rev. Lett.* **67** 661
[10] Bennett C H, Brassard G, Crépeau C, Jozsa R, Peres A and Wootters W K 1993 *Phys. Rev. Lett.* **70** 1895
[11] Boto A N, Kok P, Abrams D S, Braunstein S L, Williams C P and Dowling J P 2000 *Phys. Rev. Lett.* **85** 2733
[12] D'Angelo M, Chekhova M V and Shih Y 2001 *Phys. Rev. Lett.* **87** 013602
[13] Bin Q, Wu Y and Lü X Y 2021 *Phys. Rev. Lett.* **127** 073602
[14] Ma S, Li X, Ren Y, Xie J and Li F 2021 *Phys. Rev. Res.* **3** 043020
[15] Gou C, Hu X and Wang F 2022 *Phys. Rev. A* **106** 063718
[16] Liu C, Huang J F and Tian L 2022 *Sci. China Phys. Mech. Astron.* **66** 220311
[17] Jiang S Y, Zou F, Wang Y, Huang J F, Xu X W and Liao J Q 2023 *Opt. Express* **31** 15697
[18] Wei H, Tang J and Deng Y 2024 *New J. Phys.* **26** 123024
[19] Zou F, Li Y and Liao J Q 2023 *New J. Phys.* **25** 043027
[20] Domenico G D, Pearl S, Karnieli A, Trajtenberg-Mills S, Juwiler I, Eisenberg H S and Arie A 2022 *Opt. Express* **30** 21535
[21] Kang Y H, Lin Z P, Yang J Q, Wang Y, Song J, Yang Z B and Xia Y 2023 *Opt. Express* **31** 42976
[22] Cao D Z, Zhang X Z, Wang C, Ren C, Zhang J, Li Z, Zhang S H and Wang K 2023 *Phys. Rev. A* **107** 022417
[23] Migliore A and Messina A 2022 *Ann. Phys.* **534** 2200304

[24] Mostafavi F 2024 arXiv:2405.16793 [physics.optics]

[25] Hong S, Rehman J, Kim Y S, Cho Y W, Lee S W, Jung H, Moon S, Han S W and Lim H T 2021 *Nat. Commun.* **12** 5211

[26] Hodgson H, Zhang Y, England D and Sussman B 2023 *Appl. Phys. Lett.* **122** 34001

[27] Kim S, Stohr J, Rotermund F and Ham B S 2024 arXiv:2404.00496 [quant-ph]

[28] Zanforlin U, Lupo C, Connolly P W R, Kok P, Buller G S and Huang Z 2022 *Nat. Commun.* **13** 5373

[29] Mostafavi F, Hong M, Dawkins R B, Ferdous J, Baum I, Jin R B, Lón-Montiel R de J, You C and Magaña-Loaiza O S 2025 *Appl. Phys. Rev.* **12** 011001

[30] He Z, Zhang Y, Tong X, Li L and Wang L V 2023 *Nat. Commun.* **14** 2441

[31] Bennink R S, Bentley S J and Boyd R W 2002 *Phys. Rev. Lett.* **89** 113601

[32] Bennink R S, Bentley S J, Boyd R W and Howell J C 2004 *Phys. Rev. Lett.* **92** 033601

[33] Chen X H, Wu W, Meng S Y and Li M F 2014 *Chin. Phys. B* **23** 090701

[34] Pittman T B, Shih Y H, Strekalov D V and Sergienko A V 1995 *Phys. Rev. A* **52** R3429

[35] Zhai Y H, Chen X H, Zhang D and Wu L A 2005 *Phys. Rev. A* **72** 043805

[36] Strekalov D V, Sergienko A V, Klyshko D N and Shih Y H 1995 *Phys. Rev. Lett.* **74** 3600

[37] Scarcelli G, Valencia A and Shih Y H 2004 *Europhys. Lett.* **68** 618

[38] Xiong J, Cao D Z, Huang F, Li H G, Sun X J and Wang K 2005 *Phys. Rev. Lett.* **94** 173601

[39] Luo S, Zhou Y, Zheng H, Xu W, Liu J, Chen H, He Y, Zhang S, Li F and Xu Z 2021 *Opt. Express* **29** 30094

[40] Li W and Wang Z 2022 *Opt. Express* **30** 12684

[41] Ye Z, Hou W, Ding C X, Men X J, He R J, Zhao J, Wang H B, Xiong J and Wang K 2025 *Laser Photon. Rev.* **19** 2401610

[42] Zhang D J, Wu S, Li H J, Wang H B, Xiong J and Wang K 2017 *Sci. Rep.* **7** 17372

[43] Zhao T M, Zhang H, Yang J, Sang Z R, Jiang X, Bao X H and Pan J W 2014 *Phys. Rev. Lett.* **112** 103602

[44] Lake D P, Mitchell M, Sanders B C and Barclay P E 2020 *Nat. Commun.* **11** 2208

[45] Kim H, Kwon O and Moon H S 2019 *Sci. Rep.* **9** 18375

[46] Deng Y H, Wang H, Ding X, Duan Z C, Qin J, Chen M C, He Y, He Y M, Li J P, Li Y H, Peng L C, Matekole E S, Byrnes T, Schneider C, Kamp M, Wang D W, Dowling J P, Höfling S, Lu C Y, Scully M O and Pan J W 2019 *Phys. Rev. Lett.* **123** 080401

[47] Kim H, Kim D, Park J and Moon H S 2020 *Photon. Res.* **8** 1491

[48] Bennett A J, Patel R B, Nicoll C A, Ritchie D A and Shields A J 2009 *Nat. Phys.* **5** 715

[49] Zhai L, Nguyen G N, Spinnler C, Ritzmann J, Löbl M C, Wieck A D, Ludwig A, Javadi A and Warburton R J 2022 *Nat. Nanotechnol.* **17** 829

[50] Dangel C, Schmitt J, Bennett A J, Müller K and Finley J J 2022 *Phys. Rev. Appl.* **18** 054005

[51] Hoffet F, Lowinski J, Heller L, Padrón-Brito A and de Riedmatten H 2024 *PRX Quantum* **5** 030305